



ELSEVIER

Contents lists available at ScienceDirect

Additive Manufacturing

journal homepage: www.elsevier.com/locate/addma

Nonisothermal welding in fused filament fabrication

Keith Coasey^a, Kevin R. Hart^b, Eric Wetzel^b, David Edwards^c, Michael E. Mackay^{a,d,*}^a Department of Materials Science and Engineering, University of Delaware, Newark, DE 19716, United States^b U.S. Army Research Laboratory, Materials and Manufacturing Sciences, Aberdeen Proving Ground, MD 21005, United States^c Department of Mathematical Sciences, University of Delaware, Newark, DE 19716, United States^d Department of Chemical and Biomolecular Engineering, University of Delaware, Newark, DE 19716, United States

A B S T R A C T

Fused filament fabrication (FFF), sometimes called material extrusion (ME) offers an alternative option to traditional polymer manufacturing techniques to allow the fabrication of objects without the need of a mold or template. However, these parts are limited in the degree to which the welding interface is eliminated post deposition, resulting in a decrease in the interlaminar fracture toughness relative to the bulk material. Here reptation theory under nonisothermal conditions is utilized to predict the development of healing over time, from the rheological and thermal properties of Acrylonitrile-Butadiene-Styrene (ABS). ABS is rheologically complex and acts as a gel and as such considerations had to be made for the relaxation time of the matrix which is important in predicting the degree of interfacial healing. The nonisothermal healing model developed is then successfully compared to experimental interlaminar fracture experiments at variable printing temperatures, allowing future optimization of the process to make stronger parts.

1. Introduction

Typically, when considering the manufacturing of plastic goods, there are a number of limiting factors that restrict the object geometry, functionality, and material choice of the end product. Traditionally, polymer product fabrication relied on various molding techniques and/or subtractive manufacturing. In the case of subtractive manufacturing, a product is produced by sculpting a sample of raw material to the desired shape. In this process the product is limited to materials that can be machined, limited to geometries that can be realized using the appropriate apparatus, and has the potential to generate considerable waste. The geometric constraints can mean that multiple parts have to be fabricated and assembled to create a single, complex, functional object. Factoring in potential labor costs, the production of a part or series of parts for an assembly can accrue considerable costs [1].

In polymer molding (injection molding, blow molding, rotation molding, etc.) polymer feedstock is melted in a heated chamber and then cooled to form the desired product. This technique is very rapid, is not as inherently waste producing as subtractive manufacturing, and is able to produce very high volume products. The limiting factors are that the polymer processing equipment and the molds can be very costly, with price typically scaling with complexity, limiting this form of manufacturing typically to high volume applications [2,3].

A newer technique, called additive manufacturing (AM), provides avenues of development, where the fabrication of a product is not geometrically constrained, and material choice is not as limited. In AM, products are made by exploiting material properties to induce localized

fabrication or assembly, these include but are not limited to; sequential extrudate deposition, photo-polymerization, particle sintering, and adhesive binding. A computer operated controller is used in conjunction with the localized fabrication technique to build up a product using a sequence of instructions. Fused filament fabrication (FFF) or 3D printing is a form of AM in which thin tracks of molten polymeric material (on the order of 100–250 μm thick) are sequentially deposited to form a desired object [4]. The FFF process has a drive mechanism that forces a fiber of the desired material into a heated cylindrical channel. As the fiber progresses through the section it is heated where it transitions to a polymer melt, the fiber near the channel entrance acts like a piston, pressurizing the melt to force it through a 250–500 μm diameter nozzle. The deposited molten track forms a weld with the previous layer through molecular diffusion. The high resolution of the extrudate tracks allow for an object to be fabricated with little distinction between the layers.

FFF is an attractive manufacturing option because it has low cost barriers to entry and can print a large variety of objects without re-configuration. Objects that normally required the fabrication and assembly of multiple pieces can be produced with a reduced number of steps. Parts can also be made with variable infill, potentially greatly reducing the volume of plastic consumed. An attractive prospect of this technology is the very high level of automation, meaning labor costs do not necessarily scale with production time. This is especially important for economic scalability because the time to produce one part is considerably greater than other polymer processing techniques [5].

Since it is still a relatively new technology, consideration of

* Corresponding author at: Department of Materials Science and Engineering, University of Delaware, Newark, DE 19716, United States.

<https://doi.org/10.1016/j.addma.2020.101140>

Received 19 September 2019; Received in revised form 5 February 2020; Accepted 18 February 2020

Available online 24 February 2020

2214-8604/ © 2020 Elsevier B.V. All rights reserved.

variables that influence the part strength should be considered. Unfortunately, parts made using FFF are mechanically insufficient for load intensive applications, because the primary mode of failure is the delamination of layers and subsequent crack propagation [6–8]. Most contemporary research probes the mechanical properties of FFF parts fabricated at various conditions (print temperature, layer thickness, print angle, etc.), but these are primarily tensile and flexure tests that characterize defect modulated properties, but are not representative of a more fundamental material property such as fracture toughness (however, these considerations are still quite important depending on part geometry and application) [9]. In other words, *z*-direction strength or flexural loads are biased by geometry, flaws, etc.; in contrast interlaminar fracture toughness is a more fundamental property, and as a result is a better metric for process modeling. Thomas and Rodriguez considered modeling the development of fracture strength between extruded tracks, where they applied a nonisothermal heat transfer model, and subsequently predicted the development of fracture toughness [10]. They showed that fracture toughness in FFF parts is particularly sensitive to the wetting of tracks and the resulting mesostructure. Poor surface wetting is indicated not only by void content, but by the shape of the voids as well. Recent research by Hart et al. considered not only the fracture toughness of a specimen printed at various vertical angles, but also measuring the fracture toughness of FFF specimen annealed at different conditions [11]. Thaler et al. considered the fracture toughness and material properties of ABS carbon nanotube composites [12].

Other work has considered predicting bond strength of parts made via FFF, Coogan and Kazmer simulate healing using a diffusion coefficient and its temperature dependence. They then compare the model to mechanical data and show a good correspondence. The primary difference between their work and this effort, is that here there is a deconvolution of matrix molecular relaxation from the blend relaxation, a very important consideration for structured materials which may exhibit a yield stress. Yin et al. considered predictions of healing in multi-material FFF via inter-molecular diffusion and successfully compared the results to mechanical data. Their work requires knowledge of the time to reach maximum bonding strength between the two material interface as a function of temperature [13,14].

A heat transfer model is first developed to predict the temperature at the weld plane between sequentially deposited filaments (roads). Then a nonisothermal healing model is used to predict the interlaminar fracture toughness degree of healing of FFF layers using the material and rheological properties of acrylonitrile butadiene styrene (ABS). The predictions are compared to fracture toughness measurements of both ABS samples molded under pressure (referred to as bulk), annealed FFF parts, and FFF parts at various print conditions to validate the model. The influence of other print parameters is also assessed, allowing for future optimization of the process.

2. Experimental methodology

2.1. Materials

The ABS copolymer investigated in this study was purchased from Filabot (Barre, VT). The polymer came in pellet form, and other than drying, the pellets were used as received. Pellets were dried for at least 24 h under 12 psi vacuum

2.2. Thermal Analysis

Temperature-modulated differential scanning calorimetry (DSC) was performed on samples of the ABS using a TA Instruments Discovery DSC (New Castle, DE). A 4.1 mg sample was sealed into an hermetic aluminum DSC pan to retain oxygen in the pan. A second 3.9 mg sample was sealed into a crimped aluminum DSC pan which purged most atmospheric air from the pan during normal DSC operation. The samples

were subjected to thermal equilibration at $-85\text{ }^{\circ}\text{C}$ and a modulated temperature ramp applied to $250\text{ }^{\circ}\text{C}$. The temperature amplitude was $0.239\text{ }^{\circ}\text{C}$ with an oscillatory period of 30 s, for an overall temperature ramp of $3\text{ }^{\circ}\text{C}/\text{min}$. The thermal data was processed and analyzed using the TA instruments TRIOS software. The glass transition temperature T_g was found to be $110\text{ }^{\circ}\text{C}$. However, an unusual effect was seen; when the ABS was tested when oxygen was present, such as in a sealed DSC pan, an exotherm around $200\text{ }^{\circ}\text{C}$ occurred which can be interpreted as the oxidation of polybutadiene since it is not present under a nitrogen atmosphere [15]. More details are given in the Supplementary Material.

2.3. Rheological analysis

Oscillatory rheometry was performed on the ABS using a TA instruments ARES-G2. The tests were performed using a parallel plate geometry with two 8 mm parallel plates. To determine the linear viscoelastic region (LVE) of the polymer, a strain sweep was performed from 0.01% to 100% strain at 100 rad/s. After determination of the LVE, frequency sweeps were done with frequencies ranging from 100 rad/s to 0.01 rad/s with 5% strain at different temperatures. The ABS was tested from $128\text{ }^{\circ}\text{C}$ to $140\text{ }^{\circ}\text{C}$ with $1\text{ }^{\circ}\text{C}$ increments, and from $150\text{ }^{\circ}\text{C}$ to $230\text{ }^{\circ}\text{C}$ in $10\text{ }^{\circ}\text{C}$ increments. The frequency sweep data were shifted using time-temperature superposition to a reference temperature of $160\text{ }^{\circ}\text{C}$. Additionally, time sweeps were performed on ABS for 2 h at a strain of 3% and frequency of 0.5 rad/s, the tests were performed under both air and nitrogen environments at temperatures of $170\text{ }^{\circ}\text{C}$, $190\text{ }^{\circ}\text{C}$, $210\text{ }^{\circ}\text{C}$, and $230\text{ }^{\circ}\text{C}$.

It was noted that long time tests showed a gradual increase in the storage modulus with time. This was attributed to agglomeration of the polybutadiene spheres and will not be present during printing, more details are given in the Supplementary Material.

2.4. FTIR analysis

Transmission Fourier Transform Infrared Spectroscopy (FTIR) was performed on $50\text{ }\mu\text{m}$ thin pressed ABS films on a Thermo-Nicolet Nexus 670 FTIR spectrometer (Waltham, MA) and data was processed using Thermo Scientific Omnic series software. Tests were performed between $400\text{--}4000\text{ cm}^{-1}$ with 64 integration cycles and 4 cm^{-1} resolution. As shown in the Supplementary Material, the relative amounts of each component was determined to be: 11 wt% butadiene, 9 wt% acrylonitrile and 80 wt% styrene. Additional Attenuated Total Reflectance (ATR) measurements were performed on $850\text{ }\mu\text{m}$ thick samples using the Thermo-Nicolet Nexus 670 using an ATR attachment, the diamond prism has an index of refraction of 2.4195 with an incident angle of 45° . The emissivity of the ABS was found to be 0.45, and was calculated using a protocol detailed by Okada et al. as shown in the supplementary information [16].

2.5. Single edge notched bend specimen fabrication

The samples used to test interlaminar fracture toughness are single edge notch bend (SENB) specimens. The $10 \times 20 \times 100\text{ mm}$ samples were printed using a TAZ 4 FFF printer (Aleph Objects; Loveland, CO) with a $500\text{ }\mu\text{m}$ diameter nozzle. The fiber feed material was 2.85 mm ABS filament produced using a Thermo Scientific Process 11 twin screw extruder (Waltham, MA), and extruded at $210\text{ }^{\circ}\text{C}$. The filament was reeled using a Filabot spooler, and cooled using a Filabot airpath. Samples were printed at three different nozzle temperatures T_{Hot} of $215\text{ }^{\circ}\text{C}$, $230\text{ }^{\circ}\text{C}$, and $240\text{ }^{\circ}\text{C}$, with a bed temperature of $90\text{ }^{\circ}\text{C}$. They were printed at 60 mm/s print speed, 100% infill, with a layer thickness of $250\text{ }\mu\text{m}$, and a width of $200\text{ }\mu\text{m}$ to ensure maximized infill. The models were created and sliced with the Simplify3D (Blue Ash, OH) slicing software. The prints have a uniaxial 0 degree print direction (each track is 20 mm long), and are composed of 400 layers. To induce a notch in the specimens, a pause command was initiated after the deposition of

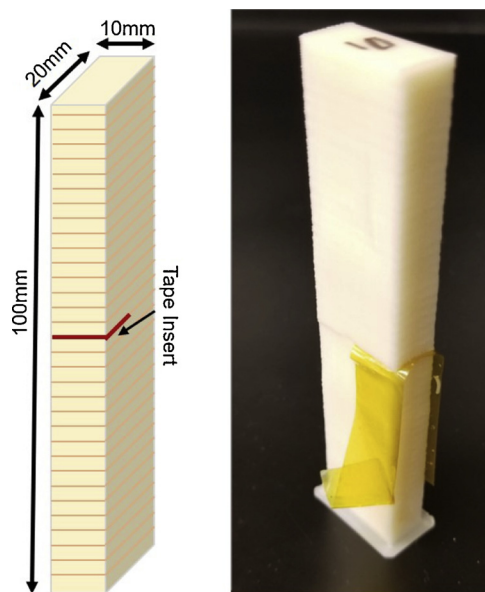


Fig. 1. (Left) Depiction of single edge notch bend sample with dimensions. (Right) Picture of a SENB specimen with the kapton tape insert.

layer 200, and 25 μm thick kapton tape was inserted approximately 10 mm into the sample (See Fig. 1). The prints were resumed manually after a pause period of about 30 s.

Bulk interlaminar fracture toughness SENB samples were fabricated using the Process 11 twin screw extruder with a slit die attachment to make a thick film. Samples were then heated and pressed at 150 $^{\circ}\text{C}$ under a pressure of 2000 psi, they were then cooled under pressure. Afterwards the pressed samples were machined to 4.5 \times 9 \times 75 mm. A 1.5 mm wide 4.5 mm long notch was then machined in the middle of each sample. A shallow precrack was then induced using a razor blade to make an indentation.

Annealed interlaminar fracture toughness SENB samples were fabricated using the annealing fixture depicted in Fig. 2. The fixture was first thermally equilibrated to 175 $^{\circ}\text{C}$. Samples (printed at 240 $^{\circ}\text{C}$) were then loaded between aluminum spacers, and the screw was tightened (lightly) to secure the samples. Printed samples were isothermally annealed for 20 h at 175 $^{\circ}\text{C}$ in an ambient environment, and afterward the oven door was opened and the samples were left to slowly cool. The annealing temperature was determined based on previous experiments done by Hart et al., where annealed samples had fracture toughness values similar to bulk material [11]. This was done to have a second



Fig. 2. The fixture used to annealing printed SENB samples. Samples are placed between metal spacers and held in place with the screw.

method of determining the bulk fracture toughness.

2.6. Tensile & SENB testing

All samples were tested using an Instron model 1122 load frame (Norwood, MA) equipped with a load cell of 2200 N capacity. Bulk material tensile samples were tested and machined in accordance to the ASTM D638 tensile properties of plastics standard, using the Type I dog bone geometry [17]. The tensile samples were loaded at a rate of 5 mm/min and the testing was recorded using a FLIR CCD camera (Wilsonville, OR) for the use of digital image correlation (DIC). Tensile testing employed the use of a speckle pattern painted on the samples to find both strain and Poisson's ratio. With the strain data and the load data, the tensile modulus was also obtained. VIC-snap and VIC-2D (Correlated Solutions, Irmo, SC) were used for the image correlations. The tensile testing here was used to characterize the tensile modulus and Poisson's ratio, necessary parameters for fracture toughness data analysis, outlined in further detail in Section 3.5. It was recognized early on that tensile testing 3D printed samples is a defect modulated mechanical property. In other words, the defects that inevitably form during printing will be failure points not allowing characterization of weld strength.

The 3D printed SENB specimens were tested according to ASTM standard E1820 for measurement of fracture toughness [18]. Based on work done by Hart et al. it was known that 3D printed ABS SENB specimens undergo a brittle fracture mode of failure, meaning linear elastic fracture mechanics can be utilized [19]. Samples were loaded in a three point bend flexure apparatus with a span of 80 mm, and the loading pins had a diameter of 6.35 mm. Samples were loaded until failure with a loading rate of 1 mm/min, images were captured using the FLIR CCD camera at a capture frequency of 1 Hz.

The bulk SENB and annealed specimens were tested in accordance to ASTM D6068 for measurement of ductile fracture failure [20]. This test was used because the overall toughness of the material included contributions from elastic failure, as well as plastic deformation. These samples were loaded with a span of 36 mm, using the same three point flexure apparatus described above. Samples were cyclically loaded at a loading rate of 1 mm/min to upper and lower critical displacements according to:

$$\delta_{u,i} = 0.25 + 0.2(i - 1)$$

$$\delta_{l,i} = 0.1 + 0.1(i - 1)$$

where $\delta_{u,i}$ and $\delta_{l,i}$ are the upper and lower critical displacement points respectively with units in millimeters, and i is representative of the i th loading cycle. Samples were cyclically loaded for 15 cycles or until crack propagation exceeded 3 mm. Images were captured at a frequency of 0.33 Hz and 0.25 Hz for bulk and annealed samples respectively, and all images were analyzed for crack propagation using the open source ImageJ software.

3. Result and discussion

3.1. Nonisothermal healing

Interfacial healing in polymers has been an interesting and important consideration for decades, and is described by a theoretical framework for diffusion of molten polymer molecules and the development of mechanical strength. In the FFF process a fiber is fed through a heated cylindrical tube, where it is eventually fed through a conical nozzle and extruded on top of existing layers. Upon deposition the extrudate rapidly heats the substrate layer and simultaneously cools causing a variable rate of molecular diffusion dependent on the local temperature. Isothermal welding models have been successful in describing the extent of interfacial healing for a number of different systems, and can be described using reptation dynamics [21]. Wool and

O'Connor applied reptation theory to provide a molecular theory of crack healing in polymers, in which the restoration of mechanical properties are related to the overall material properties [22].

The difficulty of modeling the FFF process is that the nonisothermal conditions result in a variable timescale of healing. Thomas and Rodriguez adapted a nonisothermal healing model from Bastien and Gillespie, which was an extension of the work of Wool and O'Connor. The model they used considered both the molecular diffusion aspect of healing, as well as the wetting kinetics to predict the development of fracture toughness [10,23]. Yang and Pitchumani developed a simplified nonisothermal welding model for thermoplastics, in their experiments they considered the lap welding strength of carbon fiber thermoplastic composites [24]. They varied the time of healing, under a variety of nonisothermal conditions, and were able to experimentally correlate degree of healing (DOH) of the composite strength or toughness to the duration of healing relative to the temperature dependent time of relaxation. This is given by the following expression

$$D^*_h = \frac{G(t)}{G_\infty} = \left[\int_0^t \frac{1}{\tau_r(T)} dt \right]^{1/2} \quad (1)$$

where D^*_h is the degree of healing, $G(t)$ is the time dependent toughness, G_∞ is the bulk toughness, t is time, and $\tau_r(T)$ is the temperature (T) dependent relaxation time. We will use this model to predict the degree of healing in FFF.

3.2. Comparison to thermographical data

We can model the temperature of printed interfaces as a function of time using an analytical solution to the Fourier field equation and corresponding heat transfer correlations, this is elaborated in the supplementary information. In order to employ the heat transfer model, it must be validated to see if it accurately describes the cooling of the extrudate layers at the interface. Seppala and Migler recently used infrared thermography to measure the temperature profile of ABS tracks extruded in FFF [26]. Their printer nozzle temperature T_{Hot} was held at 230 °C, the bed temperature T_{Bed} was 90 °C and the initial extrudate temperature T_{Ext} was approximately 204 °C. To validate the heat transfer correlations used in our model, predictions made by the model are compared to data corresponding to the print settings used by Seppala et al. as is displayed in Fig. 3 using parameters listed in Table 1. The model predicts the experimental data fairly well, and thus describes the temperature at the interface of the deposited tracks as a function of time. The horizontal dashed line is indicative of the glass transition temperature or T_g , once the interface falls beneath this temperature, healing ceases to occur. The glass transition temperature was measured to be approximately 110 °C, details of the T_g measurement are given in the Supplementary Material.

To utilize the nonisothermal healing model, the relationship of the characteristic relaxation time to the temperature of the polymer must be understood. In the following section the rheological properties of the ABS will be modeled and the corresponding shift factors used to determine the relaxation (reptation) time as a function of temperature.

3.3. Rheological properties

In this study the storage and loss modulus were measured as a function of frequency and temperature. This allows determination of the shift factors for the range of temperatures evaluated, and the reptation time at the reference temperature of 160 °C. Unfortunately, ABS is a block copolymer blend with polybutadiene spheres in a styrene acrylonitrile (SAN) matrix and exhibits complex rheological behavior. So, it is insufficient to associate the cross over frequency of the dynamic moduli to the relaxation (reptation) time [27] since it is the SAN matrix that heals the interface (see below) the relaxation time should be representative of the SAN matrix rather than the blend.

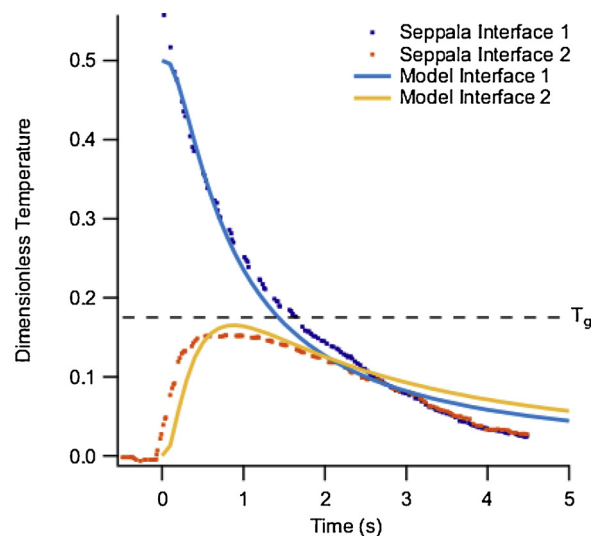


Fig. 3. The temporal temperature profile of the extrudate generated by the heat transfer model is compared to infrared thermography measured by Seppala et al. [26]. The first interface is interface 1 which is that where the hot extrudate is deposited onto the substrate material (this is $\zeta = 1$ in the Supplementary Material) and the interface below the first is interface 2 ($\zeta = 2$). The dimensionless temperature is the given temperature less that of the bed all divided by the extrudate temperature less the bed temperature (it can have a range from zero to one) and the horizontal dashed line represents the glass transition temperature.

Depending on the radii and size distribution of butadiene spheres, the acrylonitrile and styrene grafting density, the type of dispersion of the butadiene particles, and the overall composition, the blend can have a longer relaxation time than the SAN matrix [28]. This means that there can be a large amount of variation between different grades of ABS, resulting in large differences between grades. Munstedt has shown that the rheological shift factors of a SAN matrix is independent of rubber content, so the sensitivity of the relaxation time to temperature for the SAN matrix is the same as for ABS [29]. In order to model an appropriate relaxation time, careful considerations have to be made about the structure of the ABS as well as the dynamics that actually dictate matrix molecular diffusion.

The synthesis of ABS starts with emulsification of butadiene that is later polymerized with styrene and acrylonitrile monomers. A separate styrene-acrylonitrile (SAN) copolymer is synthesized to form the matrix, the treated butadiene and the SAN are subsequently co-extruded to produce the final blend [30]. The significance of this processing is that the polymerized butadiene makes up spherical domains that have diameters ranging from 300–600 nm as shown in Fig. 4. The natural consequence is that the interdiffusion of chains and elimination of the interface between FFF tracks is determined by the relaxation time scale of the SAN matrix, since the large butadiene particles will slowly diffuse. Cole et al. did a chemical analysis of ABS print interfaces using Raman spectroscopy, and found that the butadiene to styrene ratio can undergo a significant decrease within the interface, confirming the supposition of slow butadiene particle diffusion [31]. As such, it seems intuitive to treat the blend as a colloidal suspension rather than a copolymer, where the rheological properties measured are analogous to a SAN matrix with butadiene particles. A technique has been developed here using the generalized Maxwell model to separate the rheological properties of the matrix from the overall blend to determine the relaxation time of the SAN matrix.

The SAN matrix is assumed to abide by Maxwellian mechanics and is modeled using the generalized Maxwell model (GMM) given by the following:

Table 1

List of the properties used for air and ABS in the model. For air, β is the ideal gas isothermal compressibility, α is the thermal diffusivity, μ is the viscosity, and ρ is the density [25]. For ABS, w is the printed track width, L , the track thickness, k , the thermal conductivity, ρ , the density, and C_p , the specific heat capacity.

	β (K^{-1})	α (m^2/s)	μ (Pa-s)	ρ (kg/m^3)	
Air	T_{Mean}^{-1}	3.61×10^{-5}	$1.72 \times 10^{-5} + 4.67 \times 10^{-8} \times T_{Mean}$	$1.3-3.73 \times 10^{-3} \times T_{Mean}$	
	w (m)	L (m)	k (W/mK)	ρ (kg/m^3)	C_p (J/kgK)
ABS	0.2×10^{-3}	0.25×10^{-3}	0.21	1.03×10^3	2.1×10^3

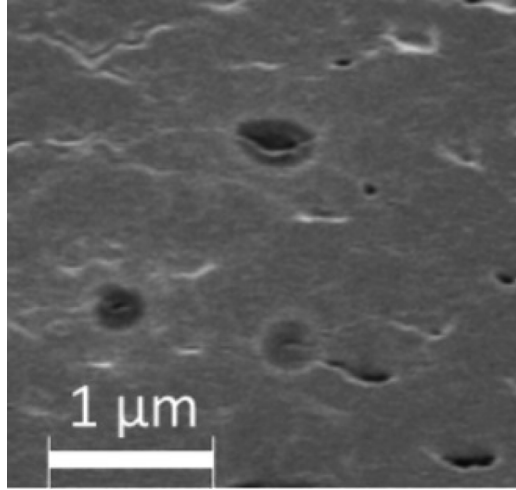


Fig. 4. SEM image of an ABS sample, the dark spherical domains are butadiene, and the gray regions are SAN rich.

$$G' = \sum_{i=1}^N G_i \frac{[\tau_i \omega]^2}{1 + [\tau_i \omega]^2} \quad G'' = \sum_{i=1}^N G_i \frac{\tau_i \omega}{1 + [\tau_i \omega]^2} \quad (2a)$$

where

$$G_N^0 = \sum_i G_i \quad (2b)$$

where G' is the storage modulus, G'' is the loss modulus, G_N^0 is the plateau modulus, τ_i is the relaxation time of each mode i , G_i is the modulus of each mode i , and ω is the oscillation frequency. The overall weighted relaxation time τ_r is defined as:

$$\tau_r = \sum_i \frac{G_i}{G_N^0} \tau_i \quad (3)$$

The value of the plateau modulus G_N^0 is taken as that of a pure SAN matrix. The overall rheological model consists of a gel-like response due to the polybutadiene spheres seen at low frequency, the GMM accounts for the matrix at intermediate frequencies and the high frequency rheological response is due to submolecular processes (such as short range interactions). Our strategy is to change the GMM parameters so the plateau modulus represents a value expected for SAN. The prediction of G' and G'' for the GMM is then subtracted from the experimental data to reveal low frequency and high frequency responses for the gel and submolecular relaxation, respectively, that are inspected to ensure this is representative of what would be expected. We also have an internal consistency check for the average relaxation time which is discussed below.

We consider the matrix to have five relaxation modes, where each subsequent mode is weighted, the weightings for the moduli and relaxation times are given by:

$$G_i = \frac{G_1}{3^{i-1}} \quad \tau_i = \frac{\tau_1}{3^{i-1}} \quad (4)$$

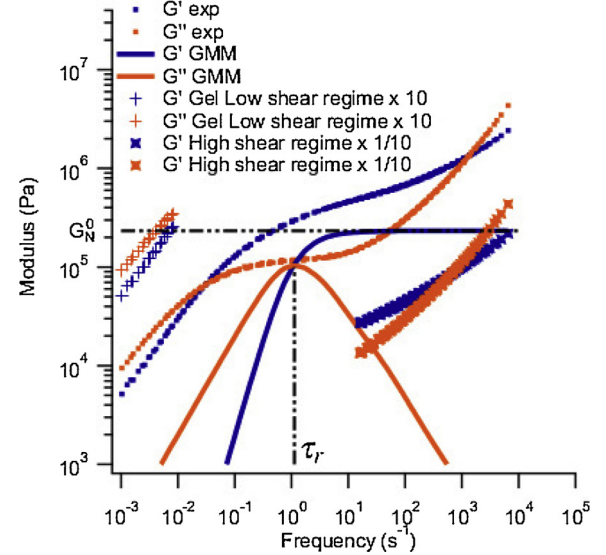


Fig. 5. The dynamic moduli for ABS is plotted as a function of frequency at a reference temperature of 160 °C. The dotted points give the rheological data, and the general Maxwell model predictions are given by the solid lines. The crosses represent the low frequency gel behavior, given by the subtraction of the GMM from the data. The x symbols represent the high frequency molecular dynamics obtained by subtracting the GMM from the data. The plateau modulus G_N^0 and the relaxation time τ_r representative of the GMM crossover frequency are indicated.

so they decrease by about half an order of magnitude for each mode. In order to fit the model to the rheological data, the values of the modulus and relaxation time for the first mode are adjusted manually. First the value of the modulus for the first mode is adjusted such that the model data are representative of the rheological data, and the experimental values for the storage and loss moduli are not exceeded, especially at high frequencies. Afterwards the relaxation time of the first mode is adjusted until the value of the weighted relaxation time τ_r (Eq. (3)) is approximately equal to the relaxation time defined by the inverse crossover frequency of the GMM moduli [27]. The rheological data as well as the data from the GMM model are plotted in Fig. 5. At low frequencies gel-like behavior is obtained by subtracting the SAN GMM model from the experimental data, and the high frequency dynamics are also obtained by subtracting the model data from the experimentally obtained data.

Gel-like behavior that has a yield stress, has been seen before by Munsted, and is presumably due to the butadiene particles [29]. The gel is clearly seen by the dynamic and loss moduli being parallel to each other [32]. The significance of this characteristic is further elaborated below.

A value of 0.170 MPa for G_1 gives a plateau modulus value of 0.254 MPa, Aoki and Tanaka demonstrated that for a pure SAN matrix the plateau modulus is about 0.3 MPa which is sufficiently consistent considering the assumptions and the fact that the SAN used here may be different to their system [33]. The value of τ_1 (1.05 s) was found to produce good agreement between the GMM crossover relaxation time

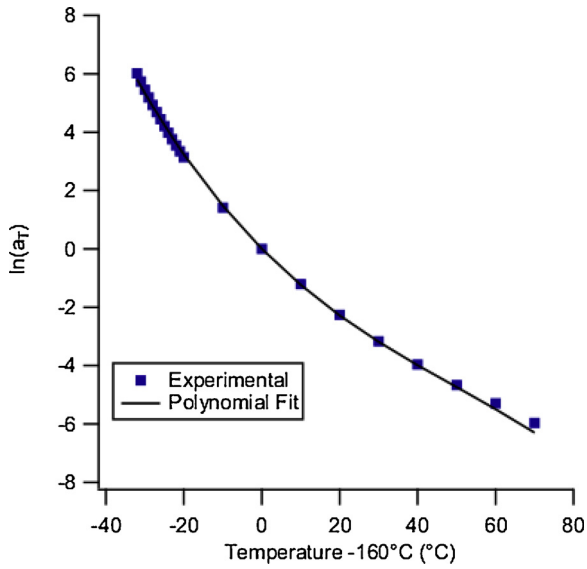


Fig. 6. The natural logarithm of the horizontal shift factors are plotted against temperature with respect to the reference temperature of 160 °C. The solid line indicates the polynomial fit.

and the weighted GMM relaxation time. The crossover frequency has a crossover relaxation time of 0.891 s while the weighted relaxation time was 0.854 s. These two times are averaged to give an overall representative relaxation time of 0.872 s for the SAN matrix at 160 °C.

From the rheological data the shift factors have been obtained for each temperature surveyed. The shift factor is representative of the sensitivity of the relaxation time to a change in temperature, with respect to a reference temperature. Normally it is sufficient to fit the shift factor data to a Williams-Landel-Ferry (WLF) equation. [34] However, due to the complex nature of the blend, there may be nonuniformities in the molecular responses of the individual components when changing temperature making a WLF fit quite difficult. Rather, a third order polynomial is used to fit the natural logarithm of the experimentally determined shift factor value given by:

$$\ln(a_T) = -7.87 \times 10^{-6}(T - 160)^3 + 0.0012(T - 160)^2 - 0.1348(T - 160) \quad (5)$$

where a_T are the shift factors used in the time-temperature-superposition (TTS) of the rheological data. The comparison of the polynomial to the data can be observed in Fig. 6 to be quite good. Multiplying this polynomial representation of a_T by the relaxation time at 160 °C allows one to determine $\tau_r(T)$ in Eq. (1).

In structured materials such as ABS, the existence of a gel-like domain can lead to complications in flow behavior. Depending on the strength and network structure of the gel, a material can exhibit an apparent yield stress, where the network must be disrupted with an applied stress before flow can occur. We note that this is highly relevant when isothermally annealing samples, as will be examined in further detail in Section 3.6. The morphology of the gel structure is yet to be determined, but is due to some network organization of the grafted butadiene particles.

The gel can be characterized in the low frequency regime using a gel strength parameter S with units Pa s^n , given by the expression [35]:

$$S = G_0 \lambda_0^n \quad (6)$$

where G_0 is the plateau modulus of the matrix, λ_0 is a network specific relaxation time, and n is the power law index. The storage modulus G' and loss modulus G'' can be modeled in the gel regime using the following:

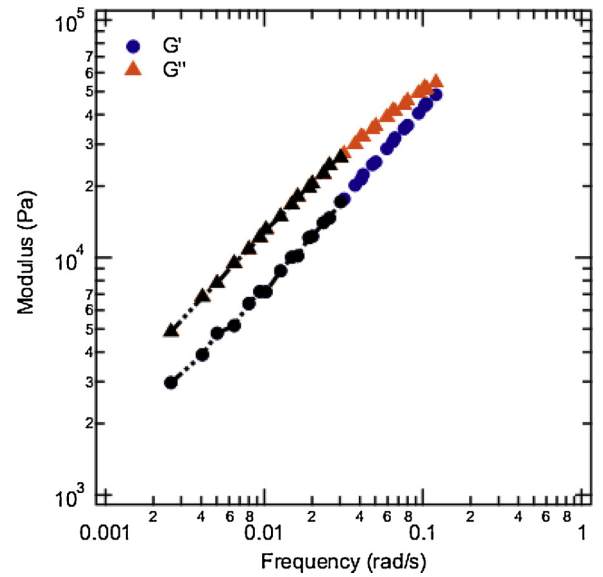


Fig. 7. Dynamic moduli data is plotted as a function of frequency in the low frequency gel regime for ABS. The reference temperature is 160 °C. The gel strength parameter S and power law index n are modeled where the storage and loss modulus are most parallel indicated by the black shading of points. This corresponds to a frequency range of 0.0026 to 0.0303 rad/s.

$$G' = \frac{\pi}{2} \frac{G_0(\omega\lambda_0)^n}{\Gamma(n)\sin\left(\frac{n\pi}{2}\right)} \quad G'' = \frac{\pi}{2} \frac{G_0(\omega\lambda_0)^n}{\Gamma(n)\cos\left(\frac{n\pi}{2}\right)} \quad (7a)$$

where

$$\tan(\delta) = \frac{G''}{G'} = \tan\left(\frac{n\pi}{2}\right) \quad (7b)$$

The power law index n is determined using Eq. (7b) in the region where G' and G'' are parallel, or where $\tan(\delta)$ is constant, this corresponds to a frequency range of 0.0026 to 0.0303 rad/s (Fig. 7). Substituting Eqn. (6) into Eq. (7) yields Eq. (8)[32]

$$G' = \frac{\pi}{2} \frac{S\omega^n}{\Gamma(n)\sin\left(\frac{n\pi}{2}\right)} \quad G'' = \frac{\pi}{2} \frac{S\omega^n}{\Gamma(n)\cos\left(\frac{n\pi}{2}\right)} \quad (8)$$

We model the low frequency gel behavior of ABS using Eq. (8), adjusting gel strength parameter S to fit G' and G'' to the experimental data. Here a n value of 0.701 and a S value of 145 kPa s^n is noted. Accepting G_0 as the matrix plateau modulus (254 kPa), using Eq. (6) λ_0 is determined to be 0.45 s, which is large considering Halley and Mackay [35] found crosslinked polyethylene had much smaller values of λ_0 ranging from 6.4×10^{-4} to 7.5×10^{-2} s. This suggests that this ABS has a rather large gel strength and will be demonstrated to have a large influence on post process annealing.

3.4. Evaluation of extrudate temperature on DOH

As will be discussed below, of all the factors considered, the temperature at which the extrudate (T_{Ext}) emerges has the most pronounced effect on the degree of healing due to its direct relation to the reptation time. Considering this, to fabricate the most desirable parts, effort will have to be spent increasing the heat transfer to the polymer in the heated section of the printer, and printing at the highest temperatures at which degradation does not occur. Here the layers are considered to be in contact with the heated bed set at 90 °C when the air temperature is 25 °C, the material and air properties needed for the heat transfer model are given in Table 1.

As seen in Fig. 8, increasing the extrudate temperature by 20 °C from 204 °C (the temperature used by Seppala and Migler [26]) has a

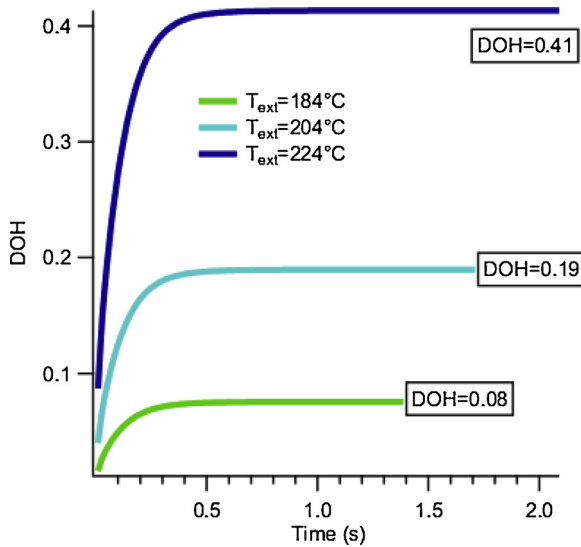


Fig. 8. Degree of healing at the interface ($\zeta = 1$) is plotted as a function of time for three different extrudate temperatures representative of layers in close proximity to the heated bed. The modeling stops when the glass transition temperature is encountered.

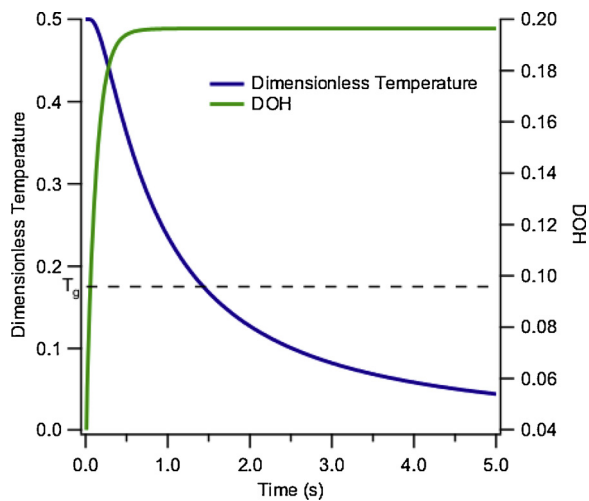


Fig. 9. Degree of healing at the interface ($\zeta = 1$) and Dimensionless Temperature are plotted as functions of time ($T_{ext} = 204^\circ\text{C}$). Most healing occurs within the first half second of cooling. The horizontal dotted line represents the glass transition temperature where healing stops. The dimensionless temperature is the given temperature less that of the bed all divided by the extrudate temperature less the bed temperature (it can have a range from zero to one).

substantial effect on both the time at which the extrudate takes to cool to the glass transition temperature, and increases the degree of healing at the interface ($\zeta = 1$) by more than a factor of two. Likewise, decreasing the temperature by 20°C to 184°C halves the overall degree of healing, and decreases the time before the extrudate cools to the glass transition temperature. What is interesting to note here is that most of the healing occurs within a half second after deposition for each of the temperatures plotted. This is more clearly illustrated in Fig. 9 where the dimensionless temperature and degree of healing are plotted against time for an extrudate temperature of 204°C . The degree of healing here is representative of a layer in intimate contact with the heated bed, this is not necessarily the case for larger prints, or for layers printed far from the bed. Note how the dimensionless temperature starts at a value of 0.5 representing a temperature halfway between the bed and extrudate temperatures as intimate contact is assumed in the model.

To check the validity of the model's ability to predict the degree of healing, FFF specimens were fabricated at different print temperatures to measure the interlaminar fracture toughness and compared this toughness value to the interlaminar fracture toughness of bulk ABS to get an indication of the degree of healing. The degree of healing is the basis of comparison between the predictions of the model and what is measured experimentally.

3.5. Interlaminar fracture toughness

FFF layers are sequentially deposited onto a growing substrate, where each layer can be treated like bulk material, but the overall object strength is limited by the periodic zones of weakness in the weld interfaces. This characteristic manifests in failure modes that are primarily dominated by crack propagation in the weld regions, the property inherent to this behavior is fracture toughness. The primary difference between bulk ABS and FFF parts is that for the bulk, failure consists of elastic crack propagation and inelastic plastic deformation, and for FFF parts failure is brittle and purely elastic. This effect has been demonstrated by Hart et al. in their studies of interlaminar fracture behavior of 3D printed parts [19]. To further elaborate, when the bulk sample is loaded, energy is dissipated into the plastic zone of the crack tip, this is demonstrated through microfibrillar alignment and yielding (crazing), cavitation of the matrix grafted butadiene particles, and localized matrix shearing which is representative of the plastic contribution [36,37]. Energy that is utilized in the extension of the crack is the linear elastic portion of the fracture toughness.

The bulk ABS SENB samples as well as the annealed ABS samples were tested in accordance to the methods used for elastic-plastic failure (ASTM E1820 & ASTM D6068), described in the supplementary information [18,20]. A load curve for one of the elastic-plastic samples is shown in Fig. 10. The image measurement tools of ImageJ were used to measure the crack extension at each critical load point, fortunately the whitening of the plastic zone of ABS provided ideal image contrast. A sequence depicting the crack growth evolution during testing is shown in Fig. 11 and Fig. 12 for bulk and annealed specimens, respectively. Using the values of crack extension along with the loading data to calculate the $J^{(i)}$ values at each critical load point, a JR curve can be constructed with $J^{(i)}$ plotted against crack extension Δa . A representative curve is shown in Fig. 13. The average value of

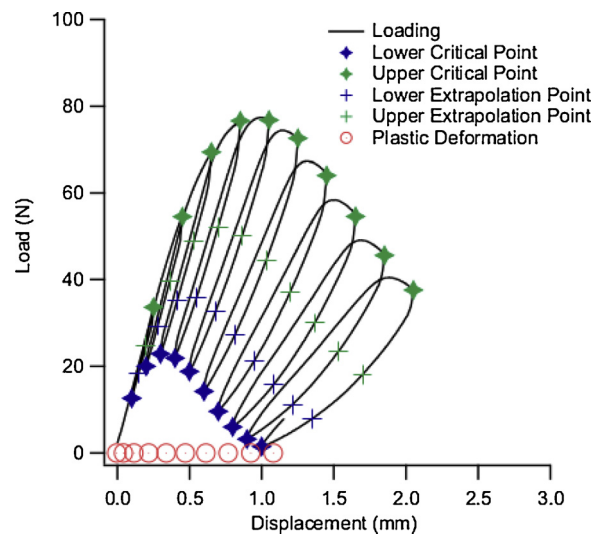


Fig. 10. A load curve of a bulk SENB sample is shown with load plotted against the crosshead displacement. The lower and upper critical load points are marked with diamonds, and the lower and upper extrapolation points are indicated with crosses. The plastic deformation points used in the calculation of the plastic toughness values are marked with the circles.

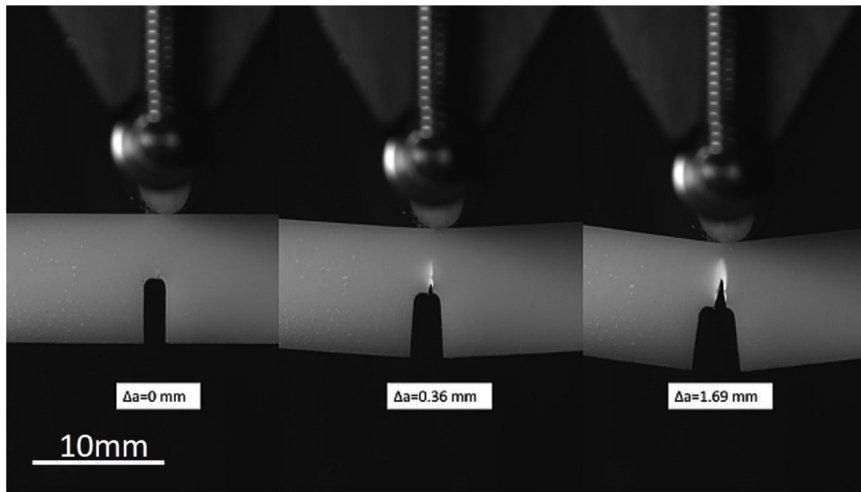


Fig. 11. Images of a bulk ABS SENB sample during testing is shown at three different crack lengths ($\Delta a = 0, 0.36,$ and 1.69 mm from left to right). The plastic stress zone whitens due to the plastic crazing and cavitation failure mechanisms.

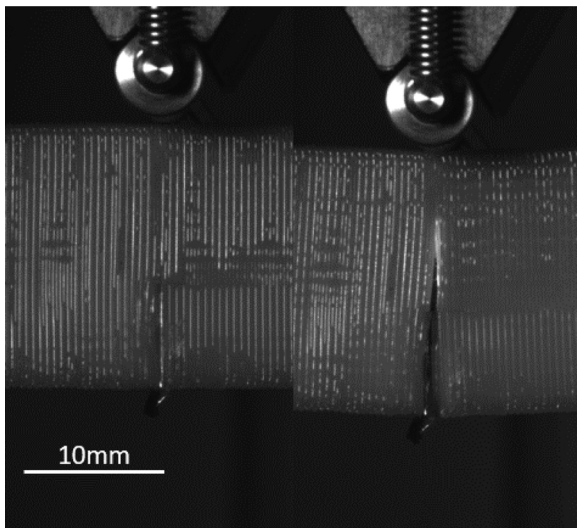


Fig. 12. Images of an annealed ABS SENB sample during testing is shown at two different crack lengths. Annealing the sample above the glass transition temperature for a sufficient amount of time causes a ductile failure response as pictured. The glossy exterior is due to oxidation of the surface.

interlaminar fracture toughness for the bulk ABS SENB specimens was found to be 2.7 ± 0.5 kJ/m², which is within reasonable proximity to a previously reported fracture toughness range of approximately 2.8–6.0 kJ/m² [36,10].

The broad range in fracture toughness for these reference values is in part due to variations in ABS formulations as described in Section 3.3. The range in values can also be due to variations in experimental implementation, such as the creation of starter cracks, and the geometry of the notch [38]. The bulk value for the samples fabricated are on the low end of this reference scale, despite using the same protocol as Hart et al. [11]. This could mean that the fabrication of the bulk ABS samples was done at an insufficient amount of time relative to the press temperature to fully anneal the samples.

As mentioned previously, it was known from experiments performed by Hart et al. that ABS FFF SENB specimens undergo linear elastic failure when processed at similar conditions. As such, it is sufficient to consider the failure of the FFF produced SENB specimens as purely elastic brittle failure. Under this assumption the elastic contribution $J_e^{(i)}$ can be defined at the point of failure, where $K^{(i)}$ is defined at a single point at the initiation of crack elongation. A single critical

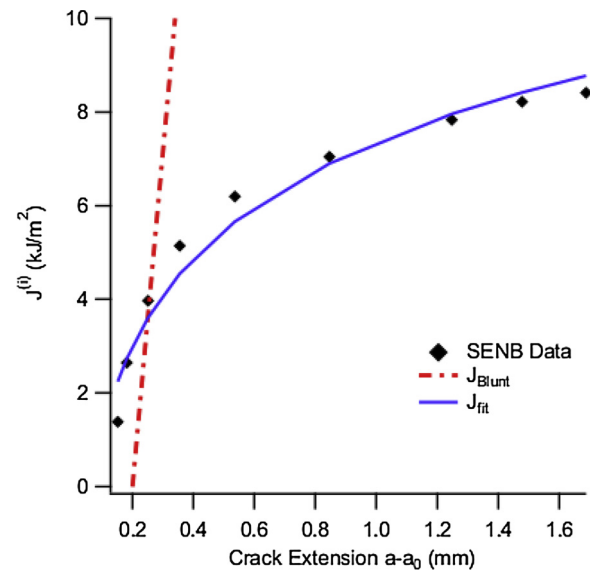


Fig. 13. JR curve of a bulk ABS SENB sample, with fracture toughness values plotted against crack extension. The black diamonds indicate experimental data, the blue line is a logarithmic fit, and the red dashed line is the blunting offset line. The intersection point is approximately 3.59 kJ/m² and represents the fracture toughness for this sample.

load value F_c or the peak load before failure, and the corresponding critical crack length a_c or the crack length just prior to failure are then used to calculate J_e , where:

$$J = J_e \tag{9}$$

An example of a load curve for the FFF SENB samples can be seen in Fig. 14, where F_c is the peak load before failure. This load curve is indicative of the failure behavior of a pure SAN matrix with no butadiene, meaning the interface is likely butadiene deficient [39]. To measure the critical crack length right before the initiation of crack propagation, image measuring tools are again utilized. Images of a FFF SENB specimen before and after brittle failure are shown in Fig. 15, note how there is no whitening at the crack tip. To calculate the degree of healing of the FFF SENB samples, the toughness of the FFF SENB samples is divided by the bulk fracture toughness value of 2.7 kJ/m² as shown in Table 2 in the ‘DOH Measured’ column.

However, an inherent assumption in the model developed here is the tracks are intimate and span the entire track width, which is not the

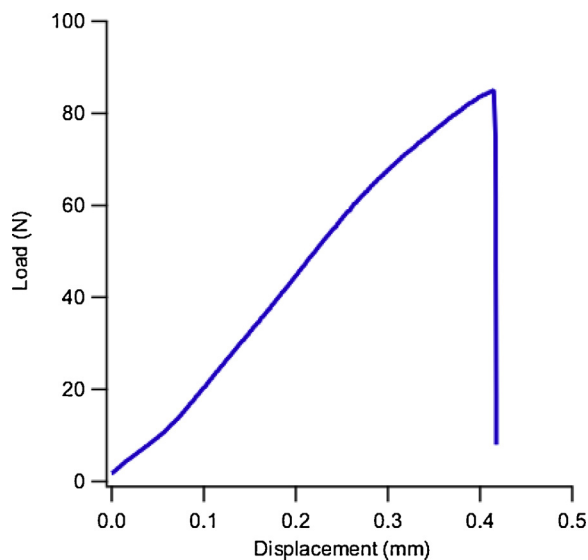


Fig. 14. Load curve for one of the FFF produced SENB samples printed at 240 °C, the sharp drop in load at failure is representative of an unstable brittle failure mode.

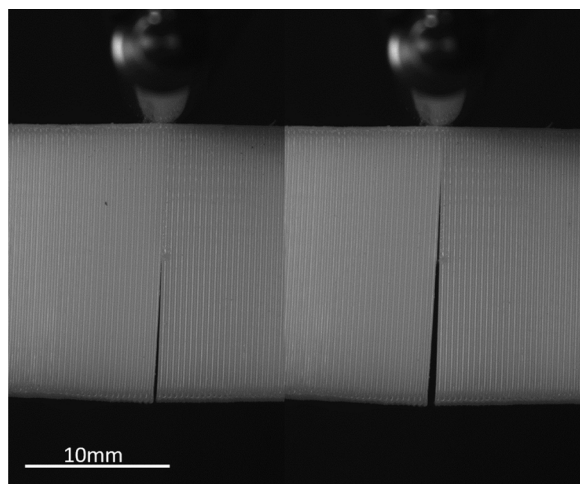


Fig. 15. Images before and after the failure of a FFF SENB specimen. Note that there is an absence of whitening ahead of the crack tip indicative of brittle failure.

Table 2

Comparison of the degree of healing as measured, when corrected for missing surface contact and the predictions made by the nonisothermal healing model.

Temperature printed (°C)	Surface contact (%)	DOH Measured (%)	DOH corrected (%)	Model DOH (%)
215	56 ± 8.7	2.7 ± 0.8	4.8 ± 1.7	3.2
230	60 ± 6.5	4.4 ± 1.3	7.3 ± 2.3	7.1
240	64 ± 8.4	6.1 ± 2.0	9.5 ± 3.3	11.4
Annealed	80 ± 8.3	28.5 ± 11.2	35.6 ± 14.4	-

case (see Fig. 16). Even though 100% infill settings were used during printing, there is voidage present in the printed sample and the contact area between tracks is smaller than the track width times its length [11]. To account for this, SENB samples were machined and cut in half to expose the cross section, and optical micrographs were taken to analyze both the surface contact between layers as well as the void content. From the image analysis tools of ImageJ, samples printed at 215 °C approximately featured 12% void content and had 56% surface

contact, 9% void content and 60% surface contact at 230 °C, and 8% void content and 64% surface contact at 240 °C. The increase in surface contact and the decrease in void content with increasing print temperature is what would be intuitively expected since the viscosity is lower at higher temperatures.

In general, the mesostructure of FFF printed structures can be quite variable, and is a strong function of the print settings and software used. The mesostructures and void shapes observed here in our samples seem to be in line with aligned and optimized printed ABS structures observed by Rodriguez et al. [40], indicating that the samples tested were representative of parts made using relatively optimized settings and a calibrated 3D printer.

When using the heat transfer model an additional consideration is that when printing the FFF SENB specimens, the fracture toughness plane being considered is 50 mm away from the bed, meaning that the temperature of the interface would be quite lower than the set bed temperature. In order to accurately model the interface an FLIR IR camera was used to measure the temperature of the interface during the pause command which was found to be approximately 55 °C when the bed is heated to 90 °C and the ambient air temperature is 25 °C. As a result, the healing is modeled using an interface temperature T_{Bed} of 55 °C rather than 90 °C. The degree of healing predictions as a function of time using the SENB printing parameters is shown in Fig. 17, and the surface contact corrected data is compared to the model predictions in Table 2. The corrected DOH is calculated by dividing the measured degree of healing by the fraction surface coverage.

The two observations most apparent from the comparison are that; the model agrees well with the experimental data, when the wetting surface contact is corrected, and the overall interlaminar fracture toughness of the SENB parts produced in a typical ambient environment is very low. Naturally, it can be inferred that the model can be used to improve the strength of FFF produced parts, and indicate the extent to which process variations improve the interlaminar welding. For instance, printing at higher temperatures greatly increases the degree of healing. Higher print temperatures allow for a greater extent of molecular diffusion, and the viscosity is lower, thus marginally increasing the surface contact of the extruded tracks.

3.6. Fracture toughness of annealed samples

Printed samples were originally annealed as a means to check the validity of the bulk molded fracture toughness values. It was seen as a method to guarantee full fracture toughness, if annealed at a temperature above the glass transition temperature for a sufficient amount of time (175 °C for 20 h) [11]. Interestingly enough, the average fracture toughness for the annealed specimen was only $771 \pm 201 \text{ J/m}^2$ before corrected for surface contact and $961 \pm 389 \text{ J/m}^2$ after correction, resulting in a degree of healing of only around 35.6% as seen in Table 2, far below the toughness of bulk material. The critical stress intensity of the annealed samples had an average value of $1.45 \text{ MPa/m}^{1/2}$ which can be compared to that of a pure injection molded SAN (80% PS 20% ACN) matrix or PS which have critical stress intensities of 2.34 and $1.93 \text{ MPa/m}^{1/2}$ respectively [39]. What this illustrates is that despite the aggressive annealing, the interface still has failure characteristics more in line with Polystyrene (PS) or a SAN matrix, than it does with ABS, furthering the notion that the interface is butadiene deficient. If treated as PS or a SAN matrix, the interface is healed to a much greater extent (closer to bulk material toughness) than when compared to ABS.

After annealing, it was expected that the voidage present between roads would coalesce. This should result in a part that would largely be indistinguishable from an injection molded specimen (no voidage between each track), disregarding the large coalesced macro voids. What is observed in Fig. 18 is a reduction in voidage (down to 1%) and an increase in surface contact (80%), but not nearly to the extent that was seen in the annealing studies done by Hart et al. [11] Meaning that the

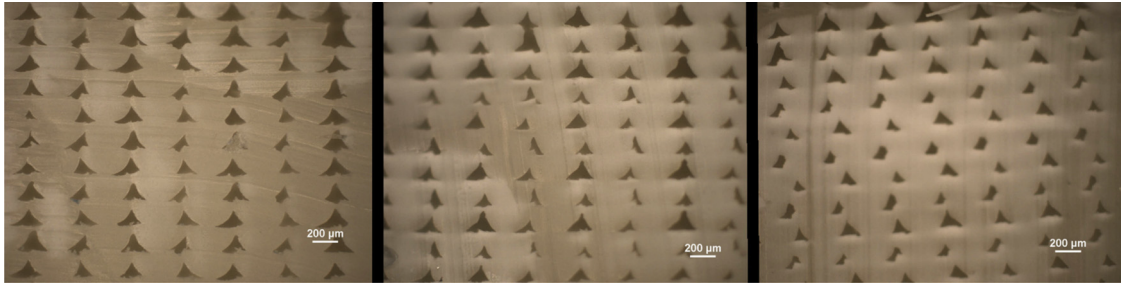


Fig. 16. Micrographs of the mesostructure and void content of SENB samples printed at 215 °C (Left), 230 °C (Middle), 240 °C (Right).

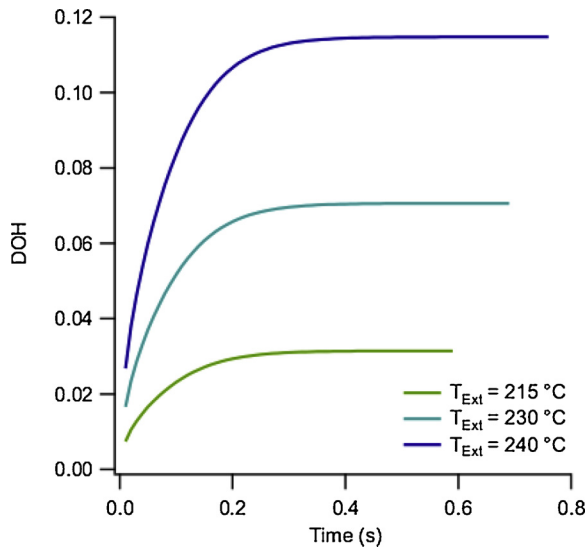


Fig. 17. Degree of healing is plotted as a function of time for the three different extrudate temperatures used in the fabrication of the FFF SENB specimens. Representative of an interface 50 mm away from the heated bed.

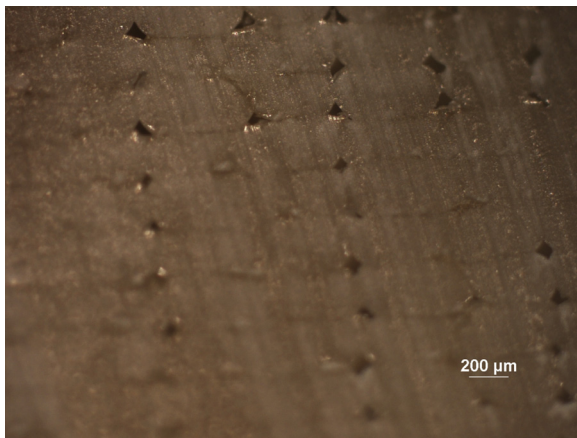


Fig. 18. Micrographs of the mesostructure and void content of an annealed SENB sample. The voids have a much greater variation of shape and size, and are not present for every track.

material properties of our grade of ABS are quite different.

What is proposed here, is that the rheological properties, and more specifically the gel-like properties of ABS, are highly influential in the annealing behavior of printed parts. Currently, isothermal annealing is the most novel technique to increase the interlaminar toughness or z-strength of printed parts, so it follows that the rheological properties of the feedstock must be fully considered for full part optimization. In Section 3.3 the gel behavior was characterized using the gel strength parameter S which had a relatively large value of 145 kPa sⁿ. Our

hypothesis is that left unperturbed, the gel structure hinders free flow, and thus retards molecular relaxation, preventing the coalescence of voidage and the diffusion of butadiene particles to the interface. The implication is that the annealing process is highly pressure sensitive, and that the gel structure must be broken or disrupted before flow and molecular diffusion can occur freely. This means that structured materials under consideration for printing must be thoroughly rheologically characterized to capture unexpected behaviors, such as the ones seen here during annealing.

3.7. Comparison to existing data

Thomas and Rodriguez considered the same welding problem and used a similar nonisothermal healing model adapted from Bastien and Gillespie [10,23]. In their work they measure the stress intensity factors (MPa-m^{1/2}) of ABS SENB samples fabricated with a Stratasys FDM1600 at various extrusion temperatures (255 °C, 270 °C, 285 °C), envelope (heated chamber) temperatures (50 °C, 60 °C, 70 °C), and track widths. To compare their results with ours it is assumed that the grade of ABS they use has the same approximate Poisson's ratio and tensile modulus, so that the stress intensity factors can be converted to fracture toughness values (kJ/m²). For the case with the lowest envelope temperature of 50 °C, the lowest extrusion temperature 255 °C results in an approximate toughness value of 0.73 kJ/m² (1.26 MPa-m^{1/2}), at the highest extrusion temperature of 285 °C the toughness value is approximately 1.2 kJ/m² (1.62 MPa-m^{1/2}). This is in reference to the bulk toughness value of approximately 2.8 kJ/m² from a reported critical stress intensity factor of 2.47 MPa-m^{1/2}.

After making fracture measurements at a variety of processing conditions, they used nonlinear regression to fit their predictions to existing data. As a result, their predictions correspond very closely with the experimental data except at the lowest print temperature. We have compared our model with their data and predictions, and have used our model to make predictions of the fracture toughness under their printing conditions, these are plotted in Fig. 19.

Overall the predictions seem to overlap the measurements made by them at higher printing conditions, with the exception of the highest printing temperature. In this regime the model overestimates the fracture toughness and gives a fracture toughness representative of bulk material. An explanation for this is that the heat transfer correlations used no longer appropriately model the extent of convection at these high temperatures. An additional assumption was that changing the substrate temperature T_{Bed} has an analogous effect to changing the environmental temperature, defined by them as T_{Env} . However, it seems that there is still a relatively wide range of print temperatures and processing conditions for which our model is valid.

Aliheidari et al. recently also characterized the fracture behavior of FFF printed ABS specimen [41]. Here they measured the fracture resistance of double cantilever beam specimen printed at different temperatures (210 °C, 230 °C, and 240 °C) using J-integral methods, but they did not correlate these results to a nonisothermal healing model. Finite element analysis methods were used to evaluate the J-integral values for the apparent fracture resistance, these values were then

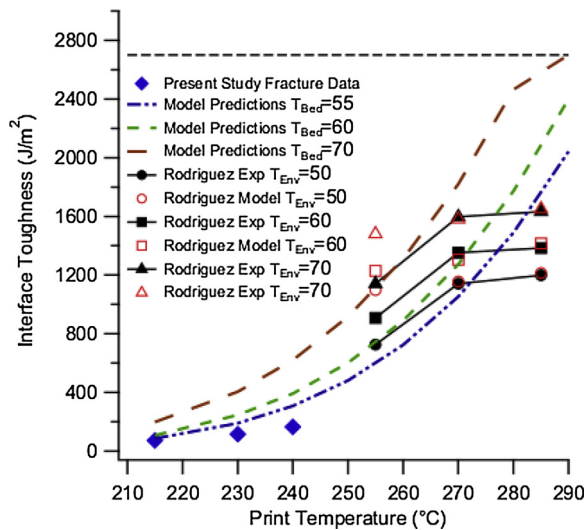


Fig. 19. Interface toughness is plotted against print temperature. The fracture values corresponding to data and predictions in the present study, are given by the diamonds in blue and dashed lines respectively. The fracture measurements are given between nozzle temperatures of 215 °C and 240 °C. The experimental data and model predictions of Thomas and Rodriguez is featured from temperatures of 255 °C to 285 °C in black and red respectively. The predictions of toughness using our model are given by the blue, green, and red dashed lines, each representative of an effective substrate temperature. The maximum fracture toughness for the ABS used here is 2700 J/m² which is indicated by the dashed black line.

corrected to account for fracture surface area to give the interlayer fracture resistance (kJ/m²). At a print temperature of 210 °C they reported a fracture resistance of 2.168 ± 0.067 kJ/m², at 230 °C a fracture resistance of 3.561 ± 0.100 kJ/m², and at 240 °C a fracture resistance of 3.908 ± 0.143 kJ/m², in reference to a cited range of bulk toughness values from 3.500–5.950 kJ/m², with the conclusion that at the highest temperatures the printed parts had near perfect adhesion.

The dramatic increase in the values when comparing their healing results with our own can be attributed to several factors. The samples they fabricated had a height of 13.5 mm, and the interface was in very close proximity to the heated bed, meaning that the print interface was likely very near the bed temperature resulting in a significant increase in molecular diffusion across the interface. However, their experimental approach might be flawed in several ways. The way that they fabricate their samples does not entirely ensure that crack propagation occurs directly between two layers. In addition to this, the method of correcting for this by converting apparent fracture resistance to interlayer fracture resistance may not be representative of the interlaminar fracture toughness. The failure of a series of layers may be too complex to be able to perform a deconvolution to assess the failure between two layers. As such, it is difficult to make comparisons to our model and results. Given that the failure mode of their samples was brittle elastic failure even at the highest print temperature, near bulk fracture resistance seems very unlikely.

4. Conclusion

We have developed a model that describes the extent of non-isothermal interfacial healing in the FFF process. Through the use of heat transfer correlations applied to an analytical solution to the dimensionless Fourier field equation, it has been demonstrated that the solution describes the temperature profile of deposited ABS tracks through comparison with data acquired through the use of IR thermography. By determining the rheological properties of the desired filament material to obtain a shift factor fit that describes the dependence of the relaxation time on temperature, the nonisothermal welding

model can be used to predict the degree to which the track interface is eliminated.

We then compare healing predictions from the model to experimentally determined interlaminar fracture toughness healing data after correcting for surface contact. The fracture experiments were performed on FFF SENB specimens and bulk extruded ABS specimens. By confirming the validity of the model, the model can be used to predict how altering process parameters, such as extrudate temperature, can improve the healing of parts made using FFF, demonstrating that bulk strength may be possible if a very high print temperature is used. We additionally demonstrate the significance of rheological characterization for structured materials such as ABS, which can limit the effectiveness of post process annealing.

Conflicts of interest

The authors declare no conflicts of interest.

Acknowledgement

We are grateful for funding under U.S. Army contract number W911NF-17-2-0186.

Appendix A. Supplementary data

Supplementary data associated with this article can be found, in the online version, at <https://doi.org/10.1016/j.addma.2020.101140>.

References

- [1] T. Pereira, J.V. Kennedy, J. Potgieter, A comparison of traditional manufacturing vs additive manufacturing, the best method for the job, *Proc. Manuf.* 30 (2019) 11–18, <https://doi.org/10.1016/j.promfg.2019.02.003>.
- [2] S. Kashyap, D. Datta, Process parameter optimization of plastic injection molding: a review, *Int. J. Plast. Technol.* 19 (1) (2015) 1–18, <https://doi.org/10.1007/s12588-015-9115-2>.
- [3] Y.-M. Chen, J.-J. Liu, Cost-effective design for injection molding, *Robot. Comput.-Integr. Manuf.* 15 (1) (1999) 1–21, [https://doi.org/10.1016/S0736-5845\(99\)00005-8](https://doi.org/10.1016/S0736-5845(99)00005-8).
- [4] Y. Huang, M.C. Leu, J. Mazumder, A. Donmez, Additive manufacturing: current state, future potential, gaps and needs, and recommendations, *J. Manuf. Sci. Eng.* 137 (1) (2014), <https://doi.org/10.1115/1.4028725>.
- [5] N. Guo, M.C. Leu, Additive manufacturing: technology, applications and research needs, *Front. Mech. Eng.* 8 (3) (2013) 215–243, <https://doi.org/10.1007/s11465-013-0248-8>.
- [6] K.J. Christiyam, U. Chandrasekhar, K. Venkateswarlu, A study on the influence of process parameters on the mechanical properties of 3D printed ABS composite, *IOP Conf. Ser. Mater. Sci. Eng.* 114 (2016), <https://doi.org/10.1088/1757-899x/114/1/012109>.
- [7] C.S. Davis, K.E. Hillgartner, S.H. Han, J.E. Seppala, Mechanical strength of welding zones produced by polymer extrusion additive manufacturing, *Addit. Manuf.* 16 (2017) 162–166, <https://doi.org/10.1016/j.addma.2017.06.006>.
- [8] X. Tian, T. Liu, C. Yang, Q. Wang, D. Li, Interface and performance of 3D printed continuous carbon fiber reinforced PLA composites, *Compos. Part A: Appl. Sci. Manuf.* 88 (2016) 198–205, <https://doi.org/10.1016/j.compositesa.2016.05.032>.
- [9] W. Wu, P. Geng, G. Li, D. Zhao, H. Zhang, J. Zhao, Influence of layer thickness and raster angle on the mechanical properties of 3D-Printed PEEK and a comparative mechanical study between PEEK and ABS, *Materials* 8 (9) (2015) 5834–5846, <https://doi.org/10.3390/ma8095271>.
- [10] J. Thomas, J. Rodriguez, *11th International Solid Freeform Fabrication Symposium*, (2000).
- [11] K.R. Hart, R.M. Dunn, J.M. Sietins, C.M.H. Mock, M.E. Mackay, E.D. Wetzel, Increased fracture toughness of additively manufactured amorphous thermoplastics via thermal annealing, *Polymer* 144 (2018) 192–204, <https://doi.org/10.1016/j.polymer.2018.04.024>.
- [12] D. Thaler, N. Aliheidari, A. Ameli, Mechanical, electrical, and piezoresistivity behaviors of additively manufactured acrylonitrile butadiene styrene/carbon nanotube nanocomposites, *Smart Mater. Struct.* 28 (8) (2019) 084004, <https://doi.org/10.1088/1361-665x/ab256e>.
- [13] T.J. Coogan, D.O. Kazmer, Healing simulation for bond strength prediction of fdm, *Rapid Prototyp. J.* 23 (3) (2017) 551–561, <https://doi.org/10.1108/rpj-03-2016-0051>.
- [14] J. Yin, C. Lu, J. Fu, Y. Huang, Y. Zheng, Interfacial bonding during multi-material fused deposition modeling (fdm) process due to inter-molecular diffusion, *Mater. Des.* 150 (2018) 104–112, <https://doi.org/10.1016/j.matdes.2018.04.029>.
- [15] Y.-S. Duh, T.-C. Ho, J.-R. Chen, C.-S. Kao, Study on exothermic oxidation of

- acrylonitrile-butadiene-styrene (ABS) resin powder with application to ABS processing safety, *Polymers* 2 (3) (2010) 174–187, <https://doi.org/10.3390/polym2030174>.
- [16] T. Okada, R. Ishige, S. Ando, Analysis of thermal radiation properties of polyimide and polymeric materials based on ATR-IR spectroscopy, *J. Photopolym. Sci. Technol.* 29 (2) (2016) 251–254, <https://doi.org/10.2494/photopolymer.29.251>.
- [17] ASTM D638-14 Standard Test Method for Tensile Properties of Plastics, (2014).
- [18] ASTM E1820-15a Standard Test Method for Measurement of Fracture Toughness, (2015).
- [19] K.R. Hart, E.D. Wetzel, Fracture behavior of additively manufactured acrylonitrile butadiene styrene (ABS) materials, *Eng. Fracture Mech.* 177 (2017) 1–13, <https://doi.org/10.1016/j.engfracmech.2017.03.028>.
- [20] ASTM D6068-10 – Standard Test Method for Determining J-R Curves of Plastic Materials, (2010).
- [21] P.G.D. Gennes, Reptation of a polymer chain in the presence of fixed obstacles, *J. Chem. Phys.* 55 (2) (1971) 572–579, <https://doi.org/10.1063/1.1675789>.
- [22] R.P. Wool, K.M. O'Connor, A theory crack healing in polymers, *J. Appl. Phys.* 52 (10) (1981) 5953–5963, <https://doi.org/10.1063/1.328526>.
- [23] L.J. Bastien, J.W. Gillespie, A non-isothermal healing model for strength and toughness of fusion bonded joints of amorphous thermoplastics, *Polym. Eng. Sci.* 31 (24) (1991) 1720–1730, <https://doi.org/10.1002/pen.760312406>.
- [24] F. Yang, R. Pitchumani, Healing of thermoplastic polymers at an interface under nonisothermal conditions, *Macromolecules* 35 (8) (2002) 3213–3224, <https://doi.org/10.1021/ma010858o>.
- [25] M.E. Mackay, *Solar Energy: An Introduction*, Oxford University Press, 2015.
- [26] J.E. Seppala, K.D. Migler, Infrared thermography of welding zones produced by polymer extrusion additive manufacturing, *Addit. Manuf.* 12 (2016) 71–76, <https://doi.org/10.1016/j.addma.2016.06.007>.
- [27] F.A. Morrison, *Understanding Rheology*, Oxford University Press, 2001.
- [28] Y. Aoki, A. Hatano, H. Watanabe, Chain relaxation time in ABS polymer melts, *Nihon Reoroji Gakkaishi* 30 (1) (2002) 59–63, <https://doi.org/10.1678/rheology.30.59>.
- [29] H. Munstedt, Rheology of rubber-modified polymer melts, *Polym. Eng. Sci.* 21 (5) (1981) 259–270, <https://doi.org/10.1002/pen.760210503>.
- [30] D.M. Considine, *Van Nostrand's Scientific Encyclopedia*, Van Nostrand Reinhold, 1995.
- [31] D.P. Cole, J.C. Riddick, H.M.I. Jaim, K.E. Strawhecker, N.E. Zander, Interfacial mechanical behavior of 3d printed ABS, *J. Appl. Polym. Sci.* 133 (30) (2016), <https://doi.org/10.1002/app.43671>.
- [32] H.H. Winter, Can the gel point of a cross-linking polymer be detected by the G'-G'' crossover? *Polym. Eng. Sci.* 27 (22) (1987) 1698–1702, <https://doi.org/10.1002/pen.760272209>.
- [33] Y. Aoki, T. Tanaka, Viscoelastic properties of miscible poly(methyl methacrylate)/poly(styrene-co-acrylonitrile) blends in the molten state, *Macromolecules* 32 (25) (1999) 8560–8565, <https://doi.org/10.1021/ma990281z>.
- [34] M.L. Williams, R.F. Landel, J.D. Ferry, The temperature dependence of relaxation mechanisms in amorphous polymers and other glass-forming liquids, *J. Am. Chem. Soc.* 77 (14) (1955) 3701–3707, <https://doi.org/10.1021/ja01619a008>.
- [35] P. Halley, M. Mackay, The gel and rheological behaviour of radiation-crosslinked linear low-density polyethylene, *Polymer* 35 (10) (1994) 2186–2191, [https://doi.org/10.1016/0032-3861\(94\)90248-8](https://doi.org/10.1016/0032-3861(94)90248-8).
- [36] M.-L. Lu, C.-B. Lee, F.-C. Chang, Fracture toughness of acrylonitrile-butadiene-styrene by J-integral methods, *Polym. Eng. Sci.* 35 (18) (1995) 1433–1439, <https://doi.org/10.1002/pen.760351803>.
- [37] A.M. Donald, E.J. Kramer, Plastic deformation mechanisms in poly(acrylonitrile-butadiene styrene) [ABS], *J. Mater. Sci.* 17 (6) (1982) 1765–1772, <https://doi.org/10.1007/bf00540805>.
- [38] M.-L. Lu, F.-C. Chang, Fracture toughness of a polycarbonate/acrylonitrile-butadiene-styrene blend by the ASTM E813 and hysteresis energy J integral methods: effect of specimen thickness and side groove, *Polymer* 36 (13) (1995) 2541–2552, [https://doi.org/10.1016/0032-3861\(95\)91199-h](https://doi.org/10.1016/0032-3861(95)91199-h).
- [39] M. Notomi, K. Kishimoto, T. Shibuya, T. Koizumi, Effects of moisture absorption on fracture behaviors of acrylonitrile-butadiene-styrene resin, *J. Appl. Polym. Sci.* 72 (3) (1999) 435–442, [https://doi.org/10.1002/\(sici\)1097-4628\(19990418\)72:3<435::aid-app13>3.0.co;2-0](https://doi.org/10.1002/(sici)1097-4628(19990418)72:3<435::aid-app13>3.0.co;2-0).
- [40] J.F. Rodriguez, J.P. Thomas, J.E. Renaud, Mechanical behavior of acrylonitrile butadiene styrene (ABS) fused deposition materials, *Exp. Investig. Rapid Prototyp.* 7 (3) (2001) 148–158, <https://doi.org/10.1108/13552540110395547>.
- [41] N. Aliheidari, R. Tripuraneni, A. Ameli, S. Nadimpalli, Fracture resistance measurement of fused deposition modeling 3d printed polymers, *Polym. Test.* 60 (2017) 94–101, <https://doi.org/10.1016/j.polymertesting.2017.03.016>.
- [42] J.R. Welty, C.E. Wicks, R.E. Wilson, *Fundamentals of Momentum, Heat, and Mass Transfer*, 3rd ed., John Wiley and Sons, 2008.
- [43] M. Corcione, Heat transfer correlations for free convection from upward-facing horizontal rectangular surfaces, *Heat Mass Transf.* 2 (2007) 48–60.
- [44] S.W. Churchill, H.H. Chu, Correlating equations for laminar and turbulent free convection from a vertical plate, *Int. J. Heat Mass Transf.* 18 (11) (1975) 1323–1329, [https://doi.org/10.1016/0017-9310\(75\)90243-4](https://doi.org/10.1016/0017-9310(75)90243-4).
- [45] R. Vadori, M. Misra, A.K. Mohanty, Studies on the reaction of acrylonitrile butadiene styrene to melt processing conditions, *Macromol. Mater. Eng.* 300 (7) (2015) 750–757, <https://doi.org/10.1002/mame.201400415>.
- [46] Y. Aoki, A. Hatano, T. Tanaka, H. Watanabe, Nonlinear stress relaxation of ABS polymers in the molten state, *Macromolecules* 34 (9) (2001) 3100–3107, <https://doi.org/10.1021/ma002076l>.
- [47] J. Haslam, H.A. Willis, *Identification and Analysis of Plastics*, J. Wiley, 1965.